

Supporting Information

**Combined experimental and theoretical studies towards mutual
Osmium–Bismuth donor/acceptor bonding**

Jacqueline Ramler,^a Krzysztof Radacki,^a Josh Abbenseth,^{b,c} and Crispin Lichtenberg^{a*}*

a: Department of Inorganic Chemistry
Julius-Maximilians-Universität Würzburg
Am Hubland, 97074 Würzburg, Germany.
Email: crispin.lichtenberg@uni-wuerzburg.de

b: Georg-August-Universität
Institut für Anorganische Chemie
Tammannstraße 4
37077 Göttingen (Germany)

c: current address
Department of Chemistry
University of Oxford,
Chemistry Research Laboratory,
12 Mansfield Road,
OX1 3TA, Oxford (UK)

Table of Contents

Single Crystal X-ray Diffraction Analysis.....	S02
Analytical Data for 3	S03
LIFDI-MS Data of [OsCl(pyr)(PNP)].....	S04
DFT calculations.....	S05
NMR Spectra of Isolated Compounds.....	S14
NMR Spectra of Reaction Mixtures.....	S16
References.....	S17

Single Crystal X-ray Diffraction Analysis

As described in the main text, crystallographic data for compound $[3\text{-}(\text{BiCl}_3)_{1.5}]_2$ does not allow the discussion of bond lengths and bond angles, and the data is only serves as a proof of connectivity. This is due twinning, for which suitable models could not be established, and significant residual electron density due to lattice-bound solvent molecules, which are severely disordered. A graphic representation of the molecular structure of $[3\text{-}(\text{BiCl}_3)_{1.5}]_2$ is given in Figure S1 (monoclinic space group, $P2_1$, $Z = 2$). One additional dimeric structure $[3\text{-}(\text{BiCl}_3)]_2$ without the BiCl_3 unit that is linked to the rest of the molecule through two $\text{Bi}\cdots\text{Cl}$ interactions is also present in the asymmetric unit.

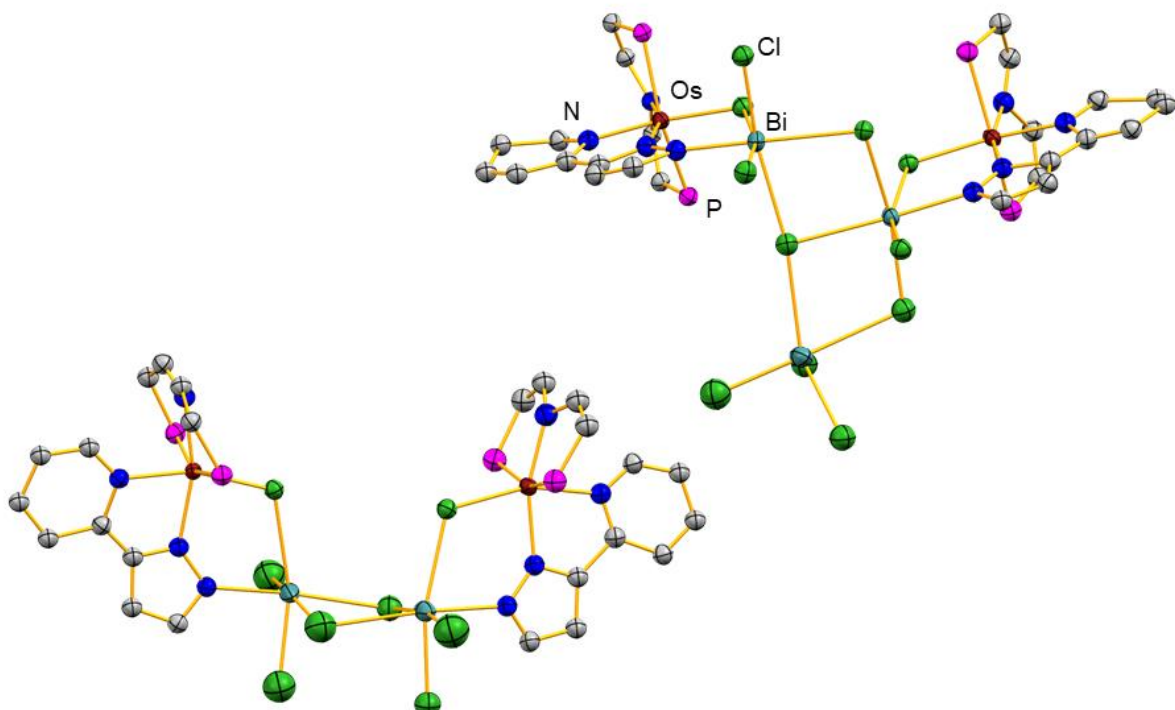
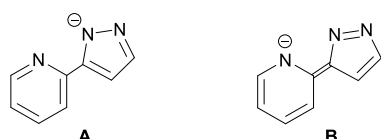


Figure S1. Molecular structures of $[3\text{-}(\text{BiCl}_3)_{1.5}]_2$ and $[3\text{-}\text{BiCl}_3]_2$ in the solid state. Hydrogen atoms and *t*Bu groups are omitted for clarity.

Resonance structure **A** is commonly observed for the monoanionic form of the pyridyl-pyrazolide ligand used in this work (Scheme S1). This is also the case in compound **2**. Major contributions by resonance structure **B** of the pyridyl-pyrazolide ligand in compound **2** are unlikely based on structural parameters of compound **2** in the solid state, as briefly discussed in the main part (Scheme S1).



Scheme S1. Resonance structures A and B of pyridyl-pyrazolide ligand.

Analytical Data for **3**

EPR spectrum of **3** conducted at 150 K showed a rhombic resonance with $g_1 = 1.498$, $g_2 = 2.095$, and $g_3 = 2.530$ and no resolved hyperfine coupling, which is in analogy to the values obtained for the literature known complex **1** (Figure S2).¹

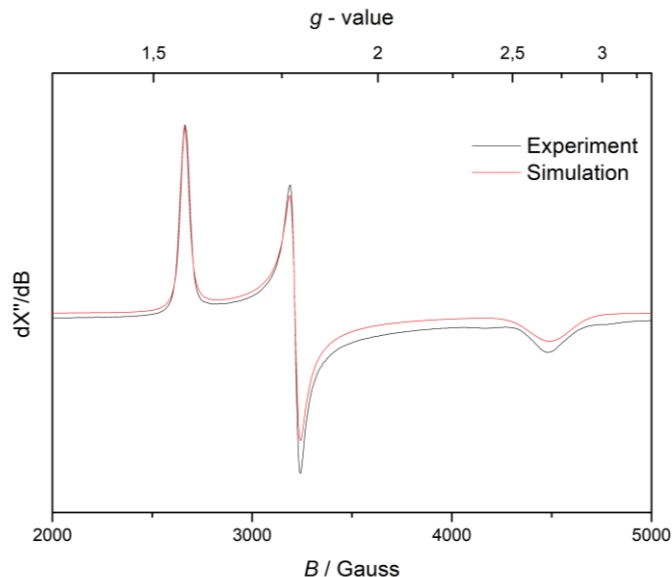


Figure S2 EPR spectrum of **3**, $g_1 = 1.498$, $g_2 = 2.095$, $g_3 = 2.530$, toluene, 150 K, 9.4324 GHz.

The redox behaviour of **3** was examined by cyclic voltammetry (Figure S3). A reversible oxidation wave was found at $E_{1/2} = -0.18$ V vs. $\text{Fc}^{0/+}$, while an irreversible and a pseudo-reversible reductive event were found at $E_{\text{pc}} = -1.40$ V and $E_{1/2} = -2.71$ V, respectively, suggesting initial chloride elimination upon reduction ($\text{Fc} = [\text{Fe}(\text{C}_5\text{H}_5)_2]$).

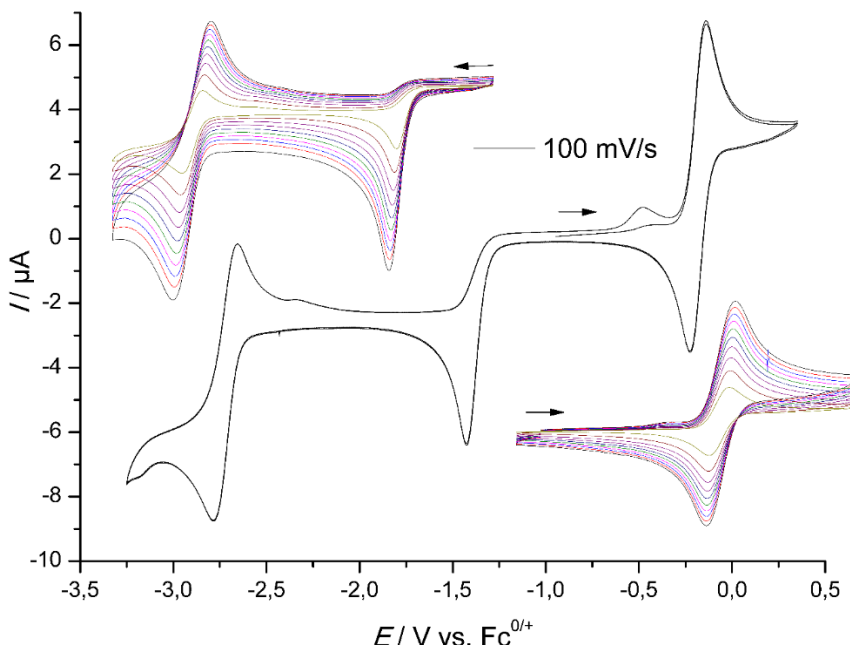


Figure S3. Cyclovoltammogram of **3** 100 mV/s, 1 mM, 0.1 M $[\text{NBu}_4][\text{PF}_6]$, THF, r.t., $E_{1/2} = -0.18$ V, $E_{\text{pc}} = -1.40$ V, $E_{1/2} = -2.71$ V, Insets: Isolated scans of the oxidative and reductive region, 1 V/s – 100 mV/s (100 mV/s steps), all potentials referenced versus ferrocene/ferrocenium.

LIFDI-MS Data of 10

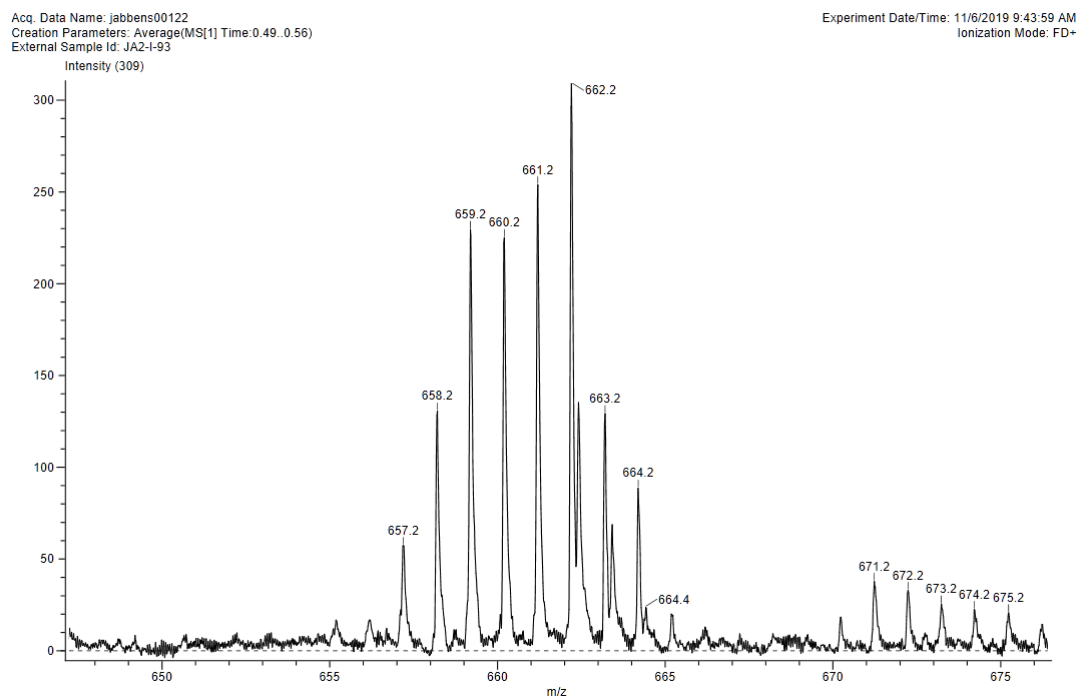
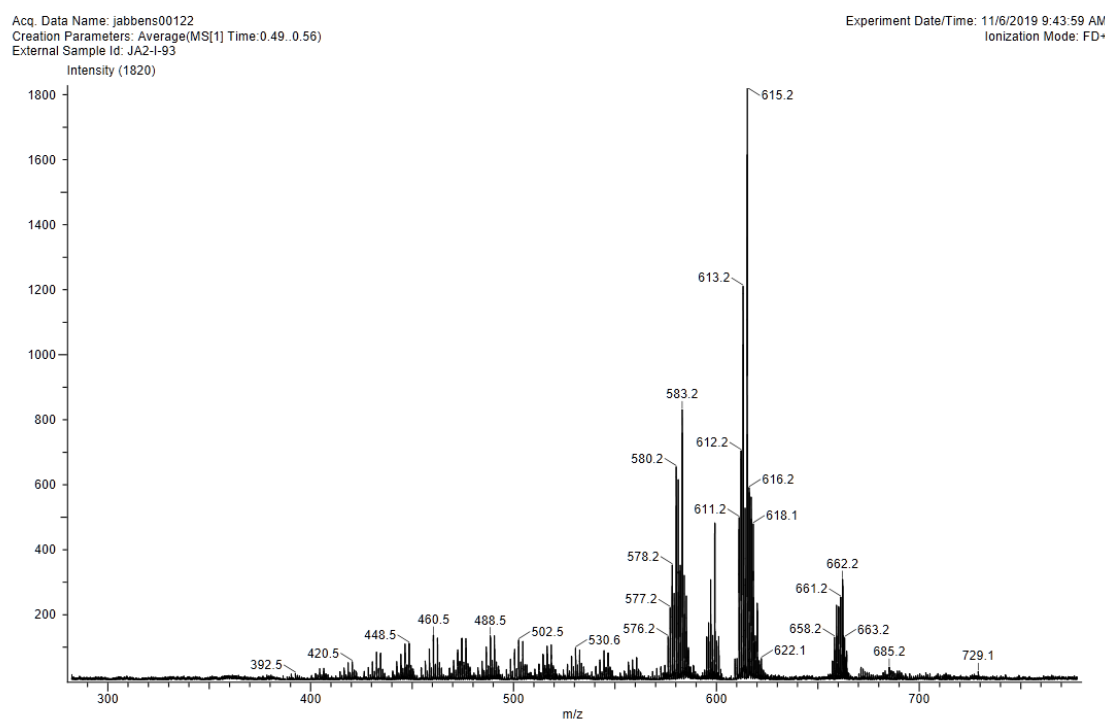


Figure S4 LIFDI-MS data of **10** in toluene, the compound decomposes during the measurement, nevertheless the $[M]^+$ peak can be observed at $m/z = 662.2$ (calcd. 662.2).

DFT Calculations

Calculations were performed with the Gaussian16 programme suite.²

Geometry optimisations of **8** gave a minimum structure with Bi···F interactions (as observed in the solid state). For comparison, an isomer without such interactions, **8b**, was also investigated and was found to also correspond to a minimum on the potential energy surface (Figure S5). Compound **8b** was found to be significantly higher in energy than **8** (H^{rel} : +19.3 kcal mol⁻¹; G^{rel} : +19.3 kcal mol⁻¹), giving evidence of the importance of Coulomb interactions in gas phase calculations.

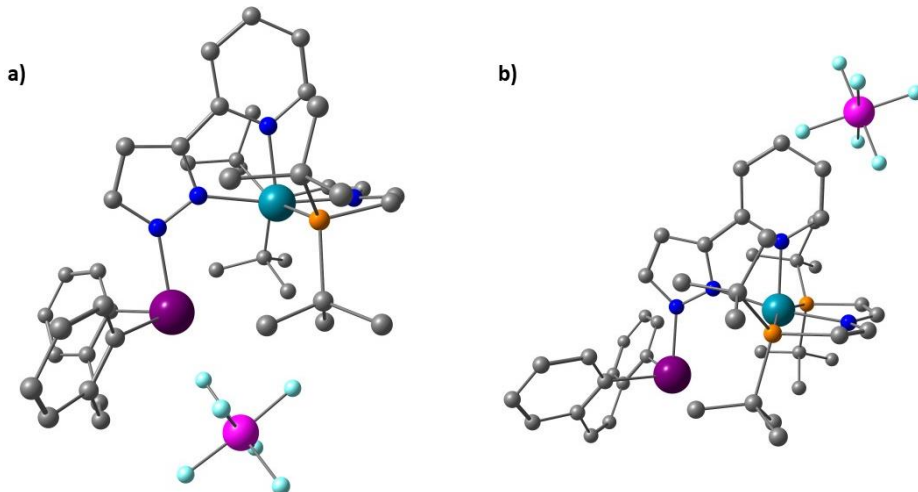


Figure S5. Molecular structures of **8** (a) and **8b** (b) as determined by DFT calculations. Hydrogen atoms are omitted for clarity.

Deletion energies for compounds **7-Me** and **8-Me**

Deletion energies (E_{del}) for compounds **7-Me** and **8-Me** were calculated (see Table 1 in main part). All donor/acceptor interactions that are due to interactions between the bismuth atom and the osmium centre or the bismuth atom and the pyrazolide-N were considered. The relevant contributions according to second order perturbation theory analyses are summarised in Table S1. Both interactions, E→Bi as well as E←Bi, were taken into account (E = Os, N), as well as interactions between the second nitrogen atom (N') of the pyrazolide moiety and the bismuth atom and between the osmium centre and the arene group in **7-Me**.

Table S1. Considered interactions for the calculation of E_{del} discussed in the main text and their corresponding donor-acceptor stabilisation energies according second order perturbation theory analyses. The associated NBO-numbers are represent by subscripts.

Compound	Os→Bi	E [kcal mol ⁻¹]	Os←Bi	E [kcal mol ⁻¹]
7-Me	p(Os) ₁₈ →p(Bi) ₁₈₀	0.06		
	d(Os) ₆₄ →σ*(Bi-C) ₂₂₇	0.81		
	d(Os) ₆₅ →σ*(Bi-C) ₂₂₇	0.16		
	d(Os) ₆₆ →p(Bi) ₁₈₀	47.01	s(Bi) ₈₅ →σ*(Os-N) ₁₈₆	5.68
	d(Os) ₆₆ →σ*(Bi-C) ₂₂₆	5.96	s(Bi) ₈₅ →σ*(Os-N) ₂₀₀	3.34
	d(Os) ₆₆ →σ*(Bi-C) ₂₂₇	1.53	s(Bi) ₈₅ →σ*(Os-P) ₂₁₆	2.56
	σ(Os-N) ₉₃ →p(Bi) ₁₈₀	0.80	σ(Bi-C) ₁₃₃ →σ*(Os-N) ₁₈₆	25.80
	σ(Os-N) ₉₃ →σ*(Bi-C) ₂₂₆	0.17	σ(Bi-C) ₁₃₃ →σ*(Os-N) ₂₀₀	0.06
	σ(Os-N) ₉₃ →σ*(Bi-C) ₂₂₇	0.09	σ(Bi-C) ₁₃₃ →σ*(Os-P) ₂₁₆	0.38
	σ(Os-N) ₁₀₇ →p(Bi) ₁₈₀	0.35	σ(Bi-C) ₁₃₄ →σ*(Os-N) ₁₈₆	0.21
	σ(Os-N) ₁₀₇ →σ*(Bi-C) ₂₂₆	0.21	σ(Bi-C) ₁₃₄ →σ*(Os-N) ₂₀₀	0.22
	σ(Os-P) ₁₂₃ →p(Bi) ₁₈₀	3.50		
	σ(Os-P) ₁₂₃ →σ*(Bi-C) ₂₂₆	0.97		
	σ(Os-P) ₁₂₃ →σ*(Bi-C) ₂₂₇	0.77		
8-Me	d(Os) ₆₂ →σ*(Bi-C) ₁₈₂	1.59		
	d(Os) ₆₂ →σ*(Bi-C) ₁₈₃	1.55	s(Bi) ₅₅ →s(Os) _{177^a}	16.33
	d(Os) ₆₃ →σ*(Bi-C) ₁₈₂	0.11	s(Bi) ₅₅ →σ*(Os-N) ₁₉₆	37.11
	d(Os) ₆₃ →σ*(Bi-C) ₁₈₃	0.12	s(Bi) ₅₅ →σ*(Os-P) ₂₄₁	0.59
	d(Os) ₆₄ →p(Bi) ₁₇₆	36.61	σ(Bi-C) ₈₉ →s(Os) _{177^a}	0.23
	σ(Os-N) ₁₀₃ →p(Bi) ₁₇₆	0.81	σ(Bi-C) ₈₉ →σ*(Os-N) ₁₉₆	1.82
	σ(Os-P) ₁₄₈ →p(Bi) ₁₇₆	2.85	σ(Bi-C) ₉₀ →s(Os) _{177^a}	0.33
	σ(Os-P) ₁₄₈ →σ*(Bi-C) ₁₈₂	0.07	σ(Bi-C) ₉₀ →σ*(Os-N) ₁₉₆	2.13
	σ(Os-P) ₁₄₈ →σ*(Bi-C) ₁₈₃	3.13		
Compound	N→Bi	E [kcal mol ⁻¹]	N←Bi	E [kcal mol ⁻¹]
7-Me	sp ² (N) ₆₂ →p(Bi) ₁₈₀	17.37		
	sp ² (N) ₆₂ →σ*(Bi-C) ₂₂₆	5.41		
	sp ² (N) ₆₂ →σ*(Bi-C) ₂₂₇	2.52		
	σ(N-N) ₉₉ →p(Bi) ₁₈₀	2.09	s(Bi) ₈₅ →σ*(N-N) ₁₉₃	0.19
	σ(N-N) ₉₉ →σ*(Bi-C) ₂₂₆	0.19	s(Bi) ₈₅ →σ*(N-C) ₁₉₇	0.80
	σ(N-N) ₉₉ →σ*(Bi-C) ₂₂₇	0.06	σ(Bi-C) ₁₃₃ →σ*(N-N) ₁₉₃	0.05
	π(N-N) ₁₀₀ →p(Bi) ₁₈₀	0.63	σ(Bi-C) ₁₃₃ →σ*(N-C) ₁₉₇	0.13
	π(N-N) ₁₀₀ →σ*(Bi-C) ₂₂₆	0.16	σ(Bi-C) ₁₃₄ →σ*(N-C) ₁₉₇	0.14
	π(N-N) ₁₀₀ →σ*(Bi-C) ₂₂₇	0.23		
	σ(N-C) ₁₀₄ →p(Bi) ₁₈₀	0.35		
	σ(N-C) ₁₀₄ →σ*(Bi-C) ₂₂₆	0.28		
8-Me	sp ² (N) ₅₈ →p(Bi) ₁₇₆	58.19		
	sp ² (N) ₅₈ →σ*(Bi-C) ₁₈₂	4.25	s(Bi) ₅₅ →σ*(N-C) ₂₀₅	1.23
	sp ² (N) ₅₈ →σ*(Bi-C) ₁₈₃	4.52	σ(Bi-C) ₈₉ →σ*(N-C) ₂₀₅	0.06
	σ(N-N) ₁₀₉ →p(Bi) ₁₇₆	4.04	σ(Bi-C) ₈₉ →π*(N-C) ₂₀₆	0.27
	σ(N-C) ₁₁₂ →p(Bi) ₁₇₆	1.49	σ(Bi-C) ₉₀ →σ*(N-C) ₂₀₅	0.06
	π(N-C) ₁₁₃ →σ*(Bi-C) ₁₈₂	0.29	σ(Bi-C) ₉₀ →π*(N-C) ₂₀₆	0.24
	π(N-C) ₁₁₃ →σ*(Bi-C) ₁₈₃	0.25		
Compound	N'→Bi	E [kcal mol ⁻¹]	N'←Bi	E [kcal mol ⁻¹]
7-Me	sp ² (N) ₆₁ →p(Bi) ₁₈₀	9.31		
	sp ² (N) ₆₁ →σ*(Bi-C) ₂₂₆	0.15		
	σ(N-C) ₉₇ →p(Bi) ₁₈₀	0.33	s(Bi) ₈₅ →σ*(N-C) ₁₉₀	0.14
	σ(N-N) ₉₇ →σ*(Bi-C) ₂₂₆	0.08		
8-Me	sp ² (N) ₅₇ →p(Bi) ₁₇₆	8.22		
	sp ² (N) ₅₇ →σ*(Bi-C) ₁₈₂	1.05		
	sp ² (N) ₅₇ →σ*(Bi-C) ₁₈₃	1.27	s(Bi) ₅₅ →σ*(N-C) ₁₉₉	0.31
	σ(N-C) ₁₀₆ →p(Bi) ₁₇₆	0.78		
Compound	Arene→Os	E [kcal mol ⁻¹]	Arene←Os	E [kcal mol ⁻¹]
7-Me	p(C) ₈₆ →σ*(Os-N) ₁₈₆	77.49	d(Os) ₆₄ →σ*(C-C) ₂₂₈	0.08
	p(C) ₈₆ →σ*(Os-N) ₂₀₀	0.07	d(Os) ₆₄ →σ*(C-C) ₂₂₉	0.06
	σ(C-C) ₁₃₅ →σ*(Os-N) ₁₈₆	1.84	d(Os) ₆₅ →σ*(C-C) ₂₂₈	0.07
	σ(C-C) ₁₃₅ →σ*(Os-N) ₂₀₀	0.05	d(Os) ₆₅ →σ*(C-C) ₂₂₉	0.22
	σ(C-C) ₁₃₆ →σ*(Os-N) ₁₈₆	1.24		

a: The non-occupied NBO-177 is composed of an osmium-centred s-orbital (66%) and an osmium-centred d-orbital(34%).

Selected NBOs relevant for Bi \rightarrow Os donor/acceptor interactions of compounds **7-Me** and **8-Me** are shown in Figure S6 and S7.

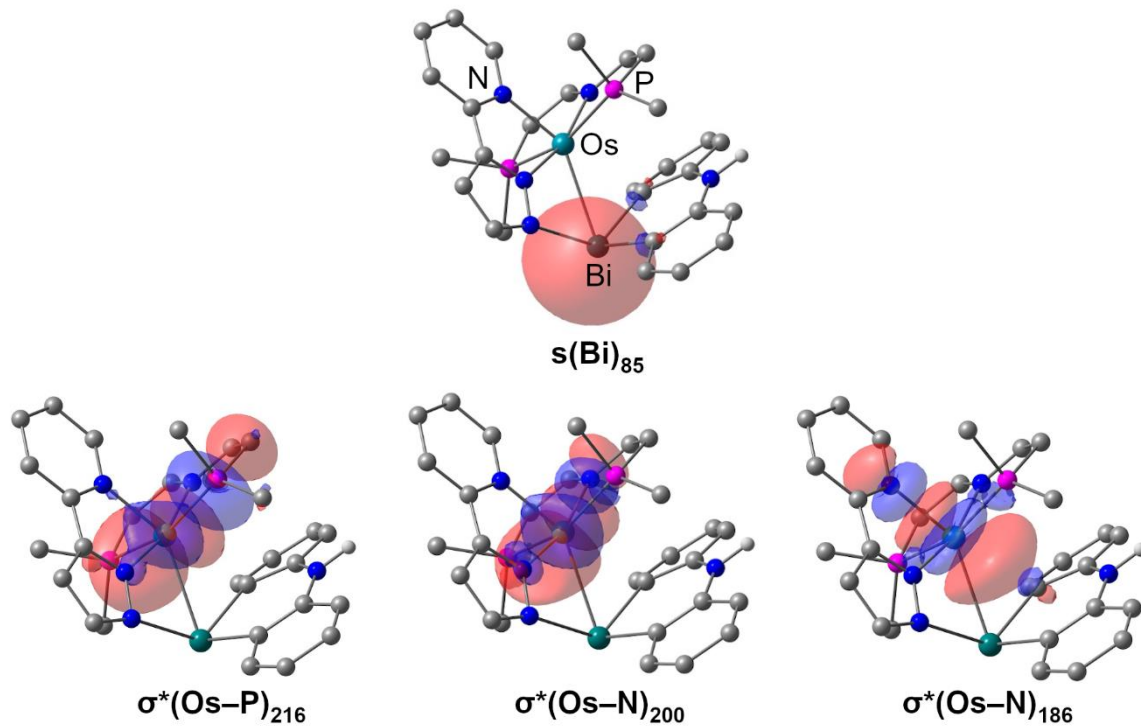


Figure S6. Selected occupied (top) and unoccupied (bottom) NBOs relevant for Bi \rightarrow Os donor/acceptor interactions of compound **7-Me**.

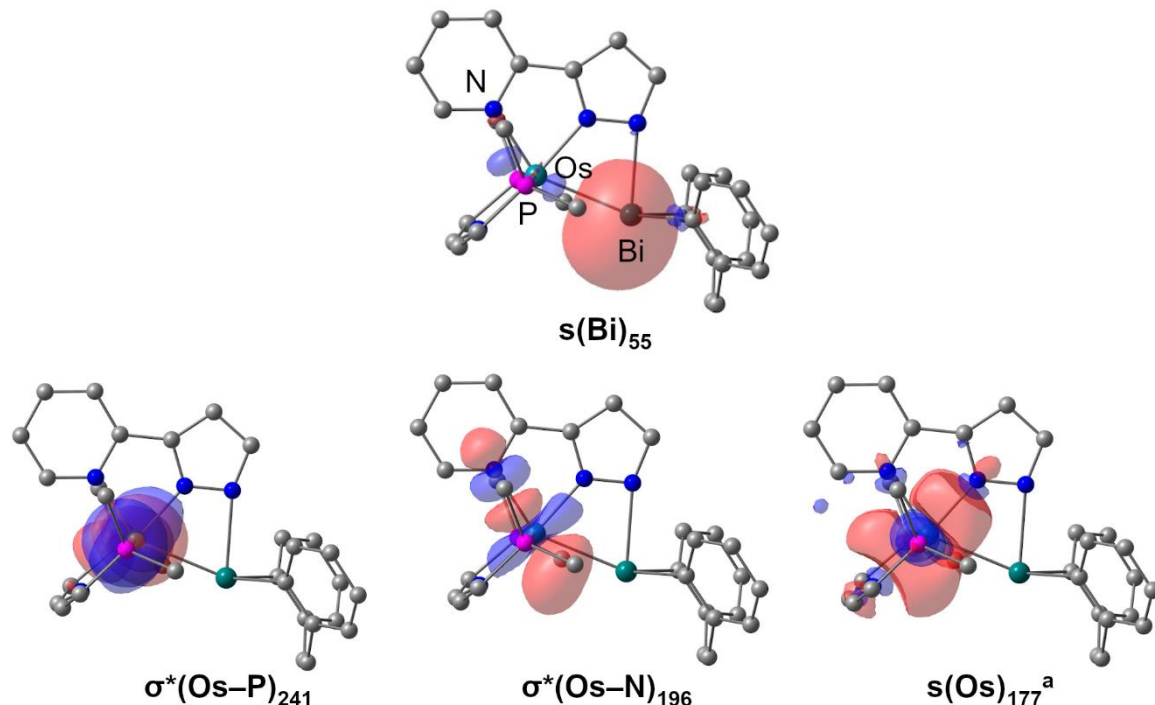


Figure S7. Selected occupied (top) and unoccupied (bottom) NBOs relevant for Bi \rightarrow Os donor/acceptor interactions of compound **8-Me**. a: The non-occupied NBO-177 is composed of an osmium-centred s-orbital (66%) and an osmium-centred d-orbital(34%).

Relaxed potential energy surface scans starting from 7-py-apical and 8

Relaxed potential energy surface scans for **7-py-apical** and **8** with decreasing Bi \cdots Os distances led to an increase in energy (Figures S8, S9). In the case of compound **8**, a slight decrease in energy was obtained during the first steps of the scan. Using the geometry of the energy minimum in Figure S9 as a starting point for geometry optimisations gave a minimum energy structure, which with a Bi–N interaction and without significant Bi–Os bonding, which was significantly higher in energy than **8** ($\Delta H = 10.3 \text{ kcal}\cdot\text{mol}^{-1}$, $\Delta G = 10.9 \text{ kcal}\cdot\text{mol}^{-1}$), the major difference being the location of the $[\text{SbF}_6]^-$ counter anion.

Similarly, relaxed potential energy surface scans for these compounds with increasing Bi \cdots N distances resulted in a steady increase in energy (not depicted).

Additional attempts to realise Bi–Os interactions in **7** and **8** by optimizing suitable starting geometries (with Bi–Os interactions) resulted in minimum structures containing only Bi–N interactions.

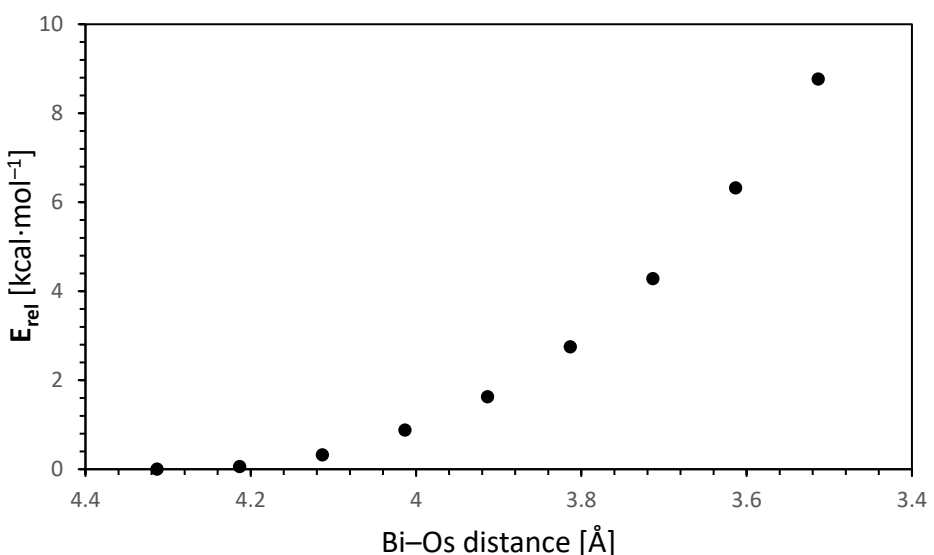


Figure S8. Relative electronic energies (E_{rel}) of **7-py-apical** with decreasing Bi \cdots Os distances as obtained from a relaxed potential energy surface scan.

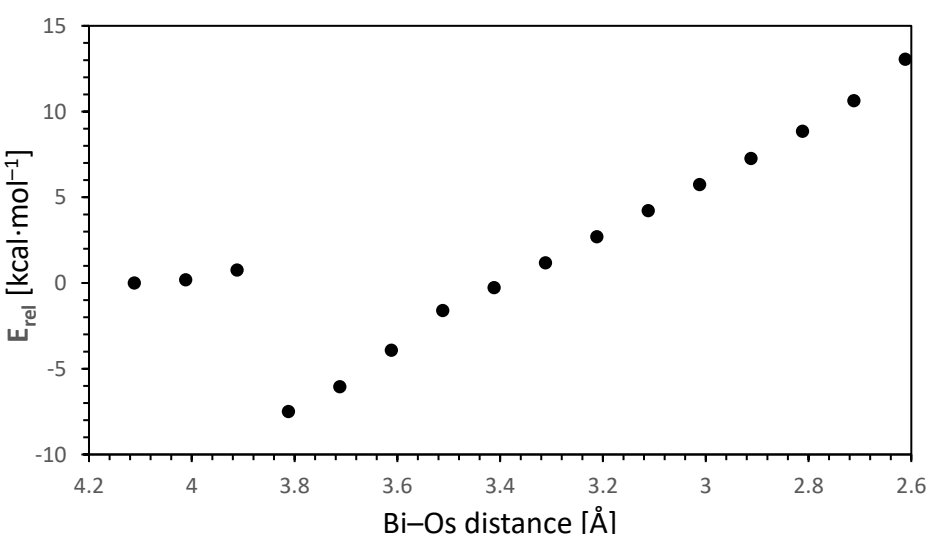


Figure S9. Relative electronic energies (E_{rel}) of **8** with decreasing Bi \cdots Os distances as obtained from a relaxed potential energy surface scan.

Relaxed potential energy surface scans starting from **7-Me** and **8-Me**

Relaxed potential energy surface scans were performed starting from the geometry of **7-Me**. In the first calculation, the Bi···Os distance was increased by 0.05 Å in each step, in a second calculation the Bi···N distance was increased by the same amount in each step (Figures S10 and S11).

Elongation of the Bi···Os distance leads to a shortening of the Bi–N bond length along with increasing energy values. After reaching a maximum, the energy values decrease, which could indicate a potential minimum geometry (Figure S10). When the last structure of the relaxed potential energy surface scan was specified as the starting geometry and an optimisation and frequency analysis was carried out, a minimum structure was obtained (compound **7-Me'**, Figure S12). **7-Me'** is slightly higher in energy than **7-Me** ($\Delta H = 2.6 \text{ kcal}\cdot\text{mol}^{-1}$, $\Delta G = 1.7 \text{ kcal}\cdot\text{mol}^{-1}$). The deletion energies for Bi···Os interactions in **7-Me'** amount to 2.7 kcal·mol⁻¹, which is significantly smaller than those in **7-Me**. (cf. main part; for corresponding donor-acceptor interaction energies from second order perturbation analyses see Tables S1-S3). A transition state, **7-Me-TS**, was located for the transformation of **7-Me** into **7-Me'** (Figure S13). **7-Me-TS** is only slightly higher in energy than the ground state **7-Me** ($\Delta H = 4.9 \text{ kcal}\cdot\text{mol}^{-1}$, $\Delta G = 5.2 \text{ kcal}\cdot\text{mol}^{-1}$).

Elongation of the Bi···N distance leads to a steady increase in energy (Figure S11).

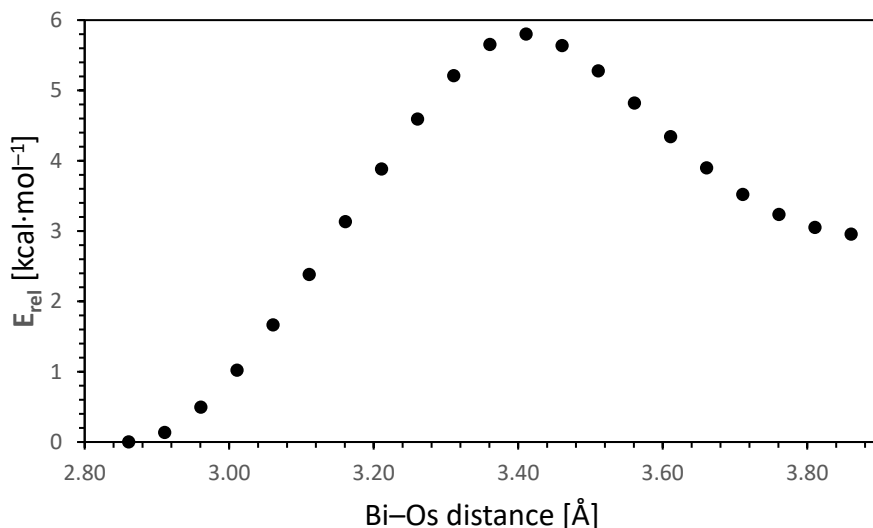


Figure S10. Relative electronic energies (E_{rel}) of **7-Me** with increasing Bi···Os distances as obtained from a relaxed potential energy surface scan.

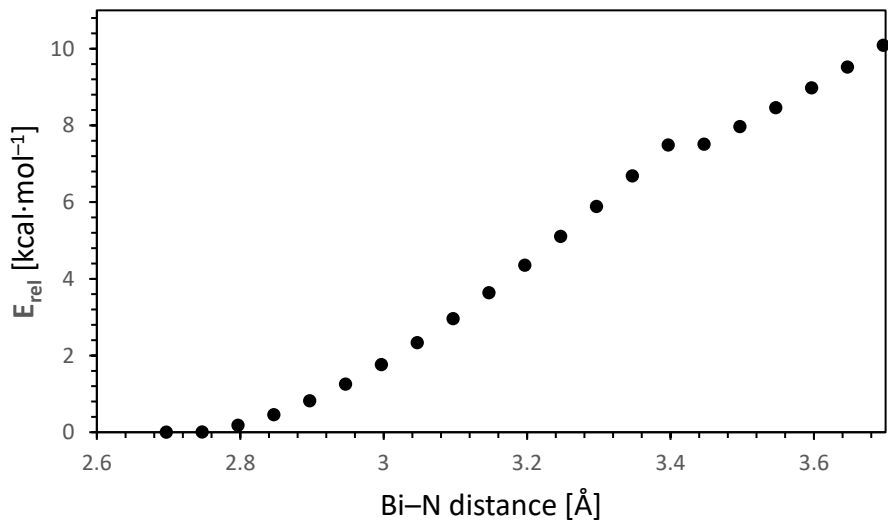


Figure S11. Relative electronic energies (E_{rel}) of **7-Me** with increasing $\text{Bi}\cdots\text{N}$ distances as obtained from a relaxed potential energy surface scan.

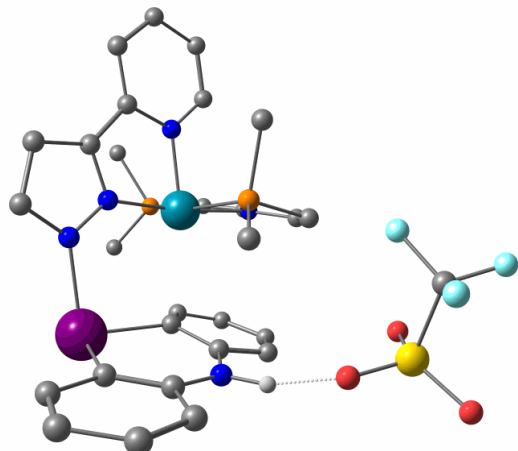


Figure S12. Calculated structure of **7-Me'**. Interatomic distances (Å): $\text{Bi}-\text{N}$, 2.288; $\text{Bi}\cdots\text{Os}$, 3.903.

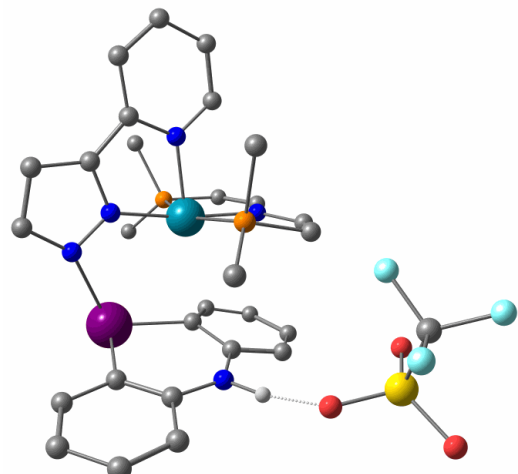


Figure S13. Calculated structure of **7-Me-TS**.

Relaxed potential energy surface scans were performed starting from the geometry of **8-Me**. The Bi···Os distance was increased by 0.05 Å in each step, in a second calculation the Bi···N distance was increased by the same amount in each step (Figures S14 and S15).

Elongation of the Bi···Os distance lowers the relative electronic energy E_{rel} to a minimum value at large Bi···Os distances > 3.5 Å (Figure S14). When the last structure of this relaxed potential energy surface scan was used as the starting geometry and an optimisation and frequency analysis were carried out, a minimum structure was obtained (compound **8-Me'**, Figure S16), which is substantially lower in energy than **8-Me** ($\Delta H = -24.5 \text{ kcal}\cdot\text{mol}^{-1}$, $\Delta G = -25.9 \text{ kcal}\cdot\text{mol}^{-1}$). The deletion energies for Bi···Os interactions in **8-Me'** amount to 1.4 $\text{kcal}\cdot\text{mol}^{-1}$, which is significantly smaller than those in **8-Me** (cf. main part; for corresponding donor-acceptor interaction energies from second order perturbation analyses see Tables S1-S3).

Elongation of the Bi···N distance leads to a steady increase in energy (Figure S15).

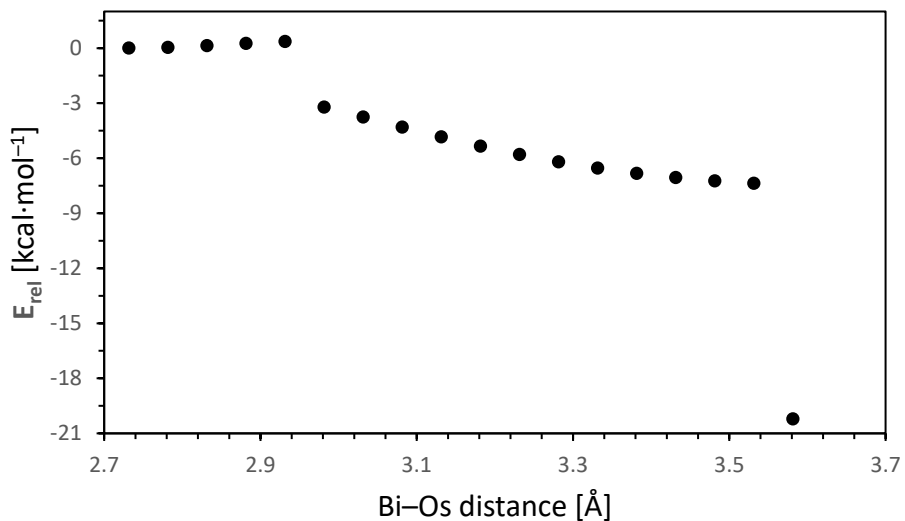


Figure S14. Relative electronic energies (E_{rel}) of **8-Me** with increasing Bi···Os distances as obtained from a relaxed potential energy surface scan.

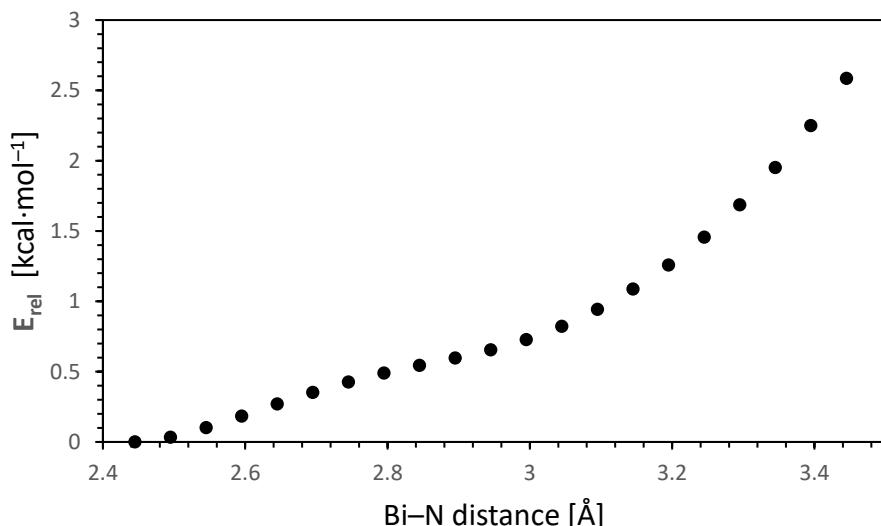


Figure S15. Relative electronic energies (E_{rel}) of **8-Me** with increasing Bi···N distances as obtained from a relaxed potential energy surface scan.

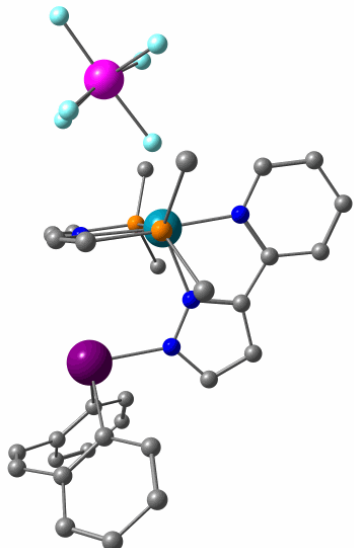


Figure S16. Calculated structure of **8-Me'**. Interatomic distances (\AA): Bi–N, 2.216; Bi–Os, 3.997.

When the $[\text{SbF}_6]^-$ anion was brought closer to the bismuth centre and the geometry thus obtained was optimised, followed by a frequency analysis, another isomer (**8b-Me'**) was obtained, which also represents a minimum on the potential energy surface (Figure S17). **8b-Me'** is energetically slightly favored compared with **8-Me** ($\Delta H = -8.9 \text{ kcal}\cdot\text{mol}^{-1}$, $\Delta G = -9.5 \text{ kcal}\cdot\text{mol}^{-1}$). The deletion energies for Bi…Os interactions in **8b-Me'** amount to 3.8 $\text{kcal}\cdot\text{mol}^{-1}$, which is significantly smaller than those in **8-Me** (cf. main part; for corresponding donor-acceptor interaction energies from second order perturbation analyses see Tables S1-S3). These findings suggest that compounds of type **7-Me** and **8-Me** show a significant number of local minima on the potential energy surface, which differ with respect to the exact nature and strength of Bi–N and Bi–Os interactions as well as the position of the $[\text{SbF}_6]^-$ counter anion.

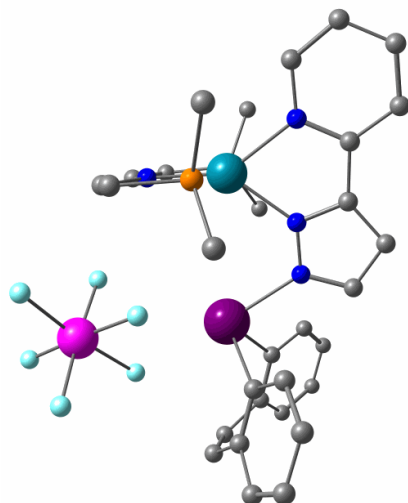


Figure S17. Calculated structure of **8b-Me'**. Interatomic distances (\AA): Bi–N, 2.310; Bi–Os, 3.840.

Table S2. Considered interactions for the calculation of E_{del} discussed above and their corresponding donor-acceptor stabilisation energies according second order perturbation theory analyses. The associated NBO-numbers are represent by subscripts.

Compound	Os→Bi	E [kcal mol ⁻¹]	Os←Bi	E [kcal mol ⁻¹]
7-Me'	d(Os) ₆₄ →p(Bi) ₁₈₀	0.58	s(Bi) ₈₅ →σ*(Os–N) ₁₈₆	0.22
	d(Os) ₆₅ →σ*(Bi–C) ₂₂₇	0.05	s(Bi) ₈₅ →σ*(Os–N) ₂₀₀	0.35
	σ(Os–N) ₁₀₇ →σ*(Bi–C) ₂₂₆	0.06	s(Bi) ₈₅ →σ*(Os–P) ₂₁₆	0.17
	σ(Os–P) ₁₂₃ →σ*(Bi–C) ₂₂₆	0.09	σ(Bi–C) ₁₃₃ →σ*(Os–N) ₁₈₆	1.81
			σ(Bi–C) ₁₃₃ →σ*(Os–N) ₂₀₀	0.71
			σ(Bi–C) ₁₃₃ →σ*(Os–P) ₂₁₆	0.16
8-Me'	d(Os) ₆₃ →p(Bi) ₁₇₆	0.81	s(Bi) ₅₅ →s(Os) ₁₇₈	1.24
8b-Me'	σ(Os–N) ₉₃ →p(Bi) ₁₇₆	0.06		
	d(Os) ₆₂ →p(Bi) ₁₇₆	1.60		
	d(Os) ₆₂ →σ*(Bi–C) ₁₈₂	0.34		
	d(Os) ₆₃ →σ*(Bi–C) ₁₈₃	0.06	s(Bi) ₅₅ →s(Os) ₁₇₇	1.55
	σ(Os–N) ₁₁₆ →p(Bi) ₁₇₆	0.09	s(Bi) ₅₅ →σ*(Os–N) ₂₀₉	0.08
	σ(Os–N) ₁₁₆ →σ*(Bi–C) ₁₈₂	0.36	s(Bi) ₅₅ →σ*(Os–P) ₂₄₁	0.11
	σ(Os–N) ₁₁₆ →σ*(Bi–C) ₁₈₃	0.14	σ(Bi–C) ₈₉ →s(Os) ₁₇₇	0.08
	σ(Os–P) ₁₄₈ →p(Bi) ₁₇₆	0.23		
	σ(Os–P) ₁₄₈ →σ*(Bi–C) ₁₈₃	0.10		

Table S3. Deletion energies E_{del} for compounds **7-Me'**, **8-Me'**, and **8b-Me'** based on the interactions given in Table S2.

Type of E_{del}	7-Me' E_{del} [kcal·mol ⁻¹]	8-Me' E_{del} [kcal·mol ⁻¹]	8b-Me' E_{del} [kcal·mol ⁻¹]
Os→Bi	0.48	0.51	2.56
Os←Bi	2.18	0.90	1.28
Sum	2.66	1.41	3.84

Energies of Compounds Investigated by DFT Calculations

The energies of compounds investigated by DFT calculations are given in Table S4. Their Cartesian coordinates are given in a separate .xyz file.

Table S4. Energies of calculated species.

Entry	Compound	ΔH [hartree]	ΔG [hartree]	Imaginary frequencies
1	2	-2086.931453	-2087.037041	none
2	5	-1980.571370	-1980.672911	none
3	6	-1614.034656	-1614.141433	none
4	pyridine	-248.203059	-248.235679	none
5	tetrahydrofuran	-232.344751	-232.379051	none
6	2-Me	-1615.469588	-1615.548528	none
7	7	-3571.118658	-3571.275403	none
8	7-py-apical	-3571.114120	-3571.270435	none
9	8	-3236.320005	-3236.480571	none
10	8b	-3236.289319	-3236.449813	none
11	7-Me	-3099.651100	-3099.774140	none
12	7-Me'	-3099.646906	-3099.772262	none
13	7-Me-TS	-3099.643247	-3099.765727	one (-61.2 cm ⁻¹)
14	8-Me	-2764.835690	-2764.967620	none
15	8-Me'	-2764.874687	-2765.008846	none
16	8b-Me'	-2764.849819	-2764.982674	none

NMR Spectra of Isolated Compounds

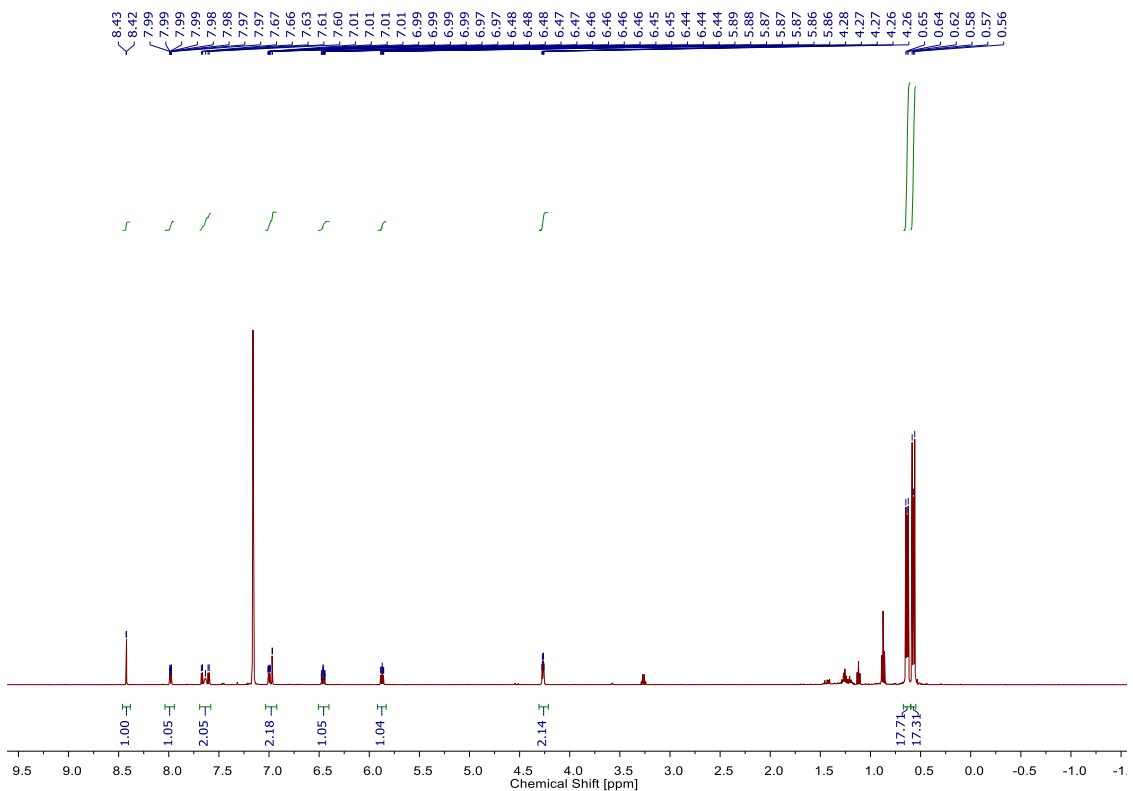


Figure S18. ¹H NMR spectrum of **2** in C₆D₆ at r.t., residual pentane and ether stems from the deuterated solvent.

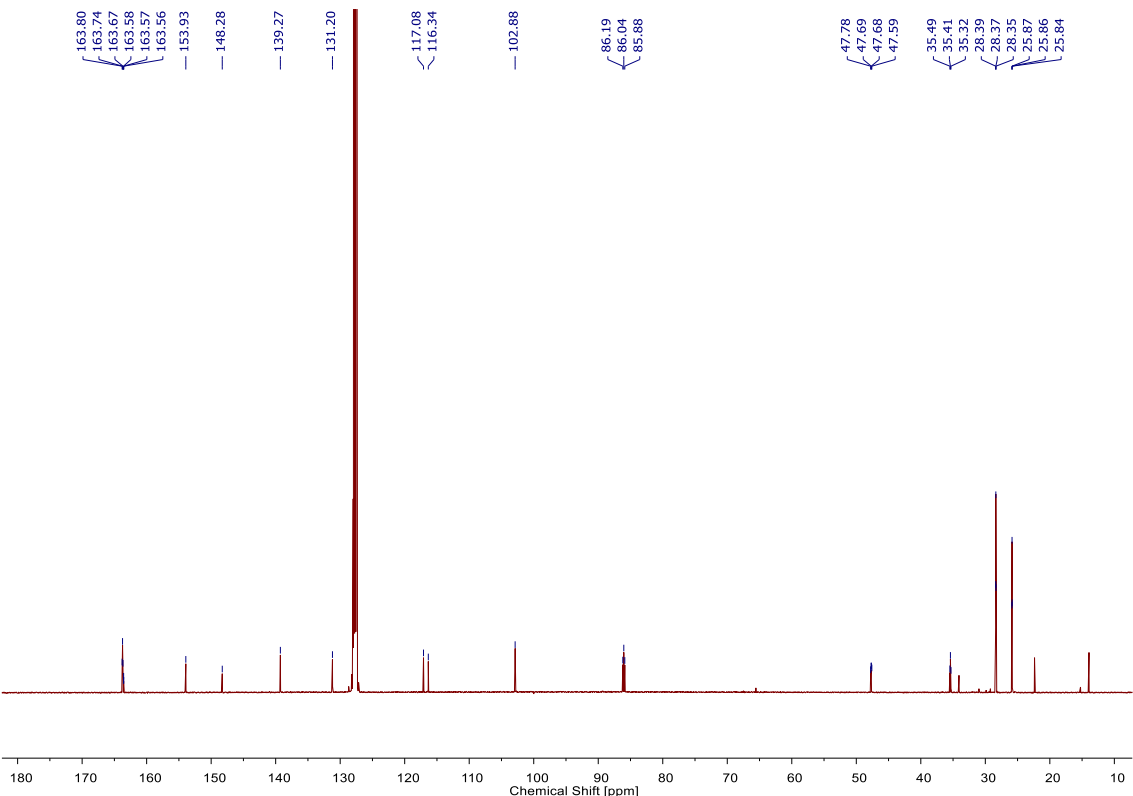


Figure S19. ¹³C{¹H} NMR spectrum of **2** in C₆D₆ at r.t.; residual pentane and diethyl ether stems from the deuterated solvent.

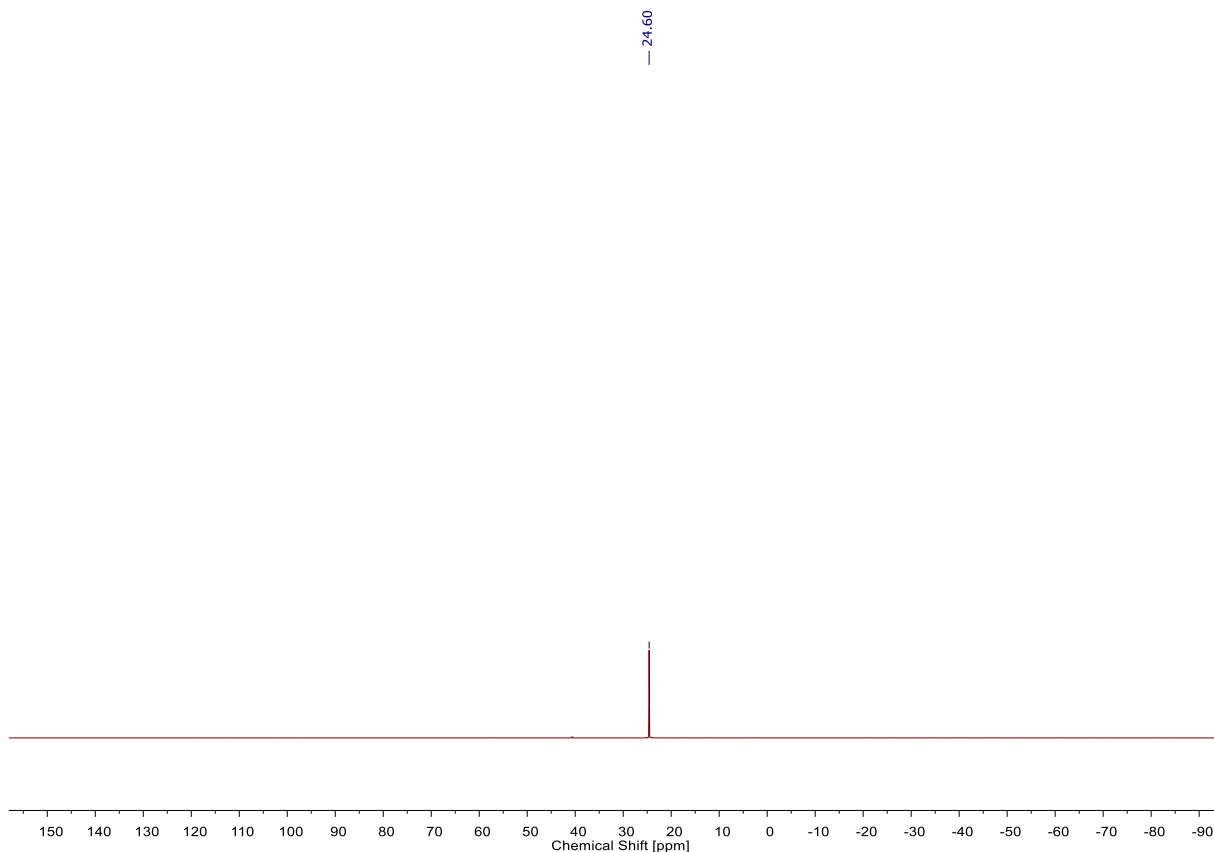


Figure S20. $^{31}\text{P}\{\text{H}\}$ NMR spectrum of **2** in C_6D_6 at r.t..

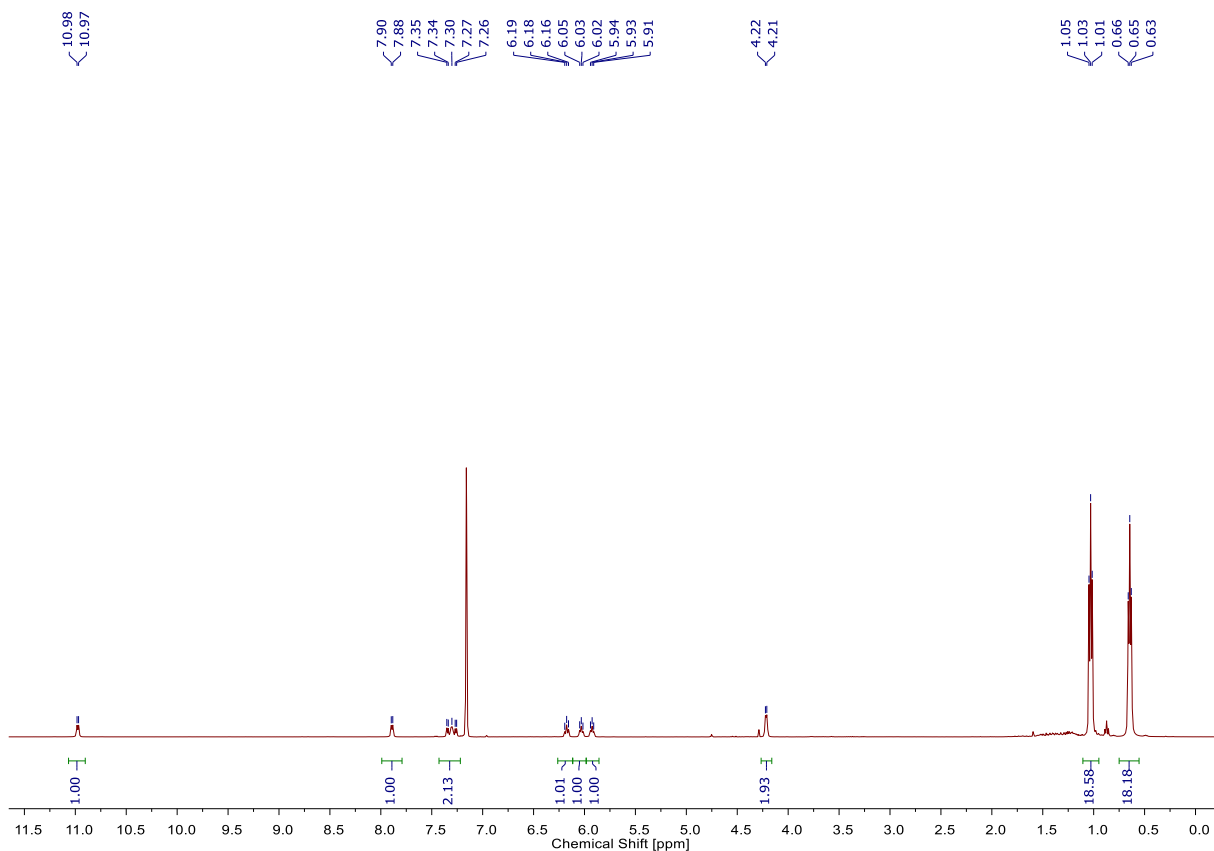


Figure S21. ^1H NMR spectrum of **10** in C_6D_6 at r.t..

NMR Spectra of Reaction Mixtures

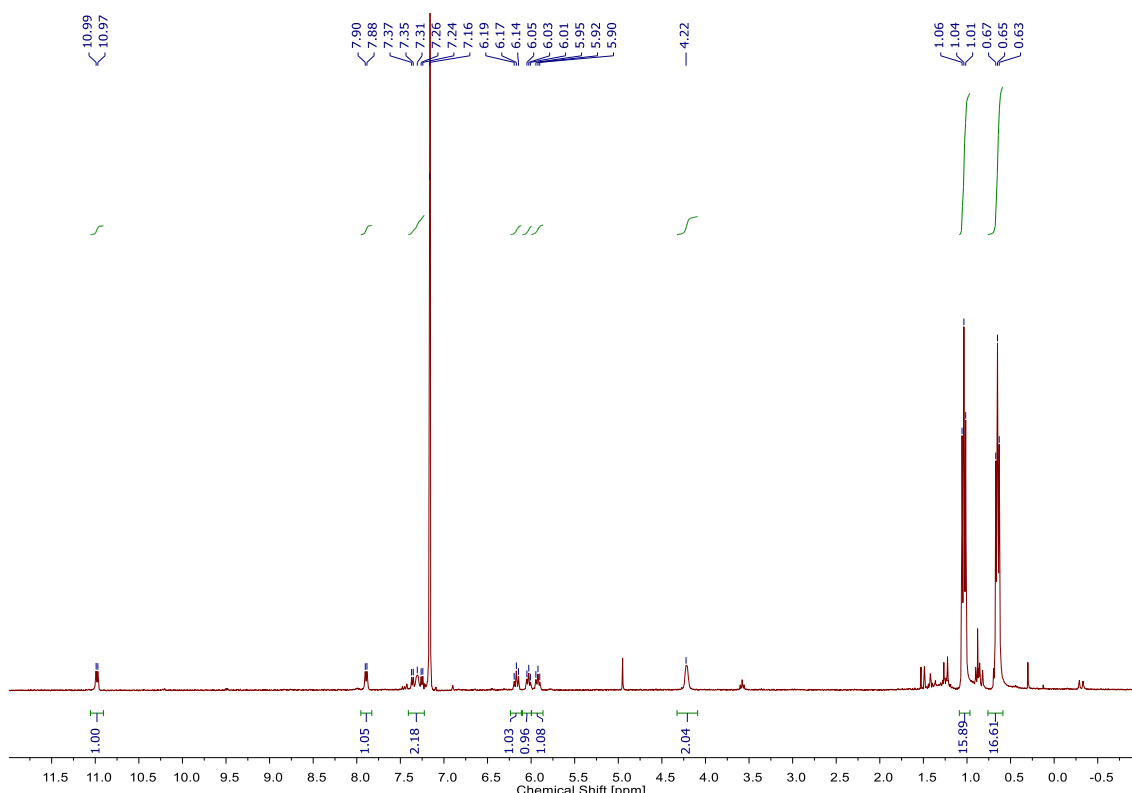


Figure S22. ¹H NMR spectrum of the reaction of **9** with **5** after benzene extraction. The spectrum was recorded at r.t. using C₆D₆ as a solvent.

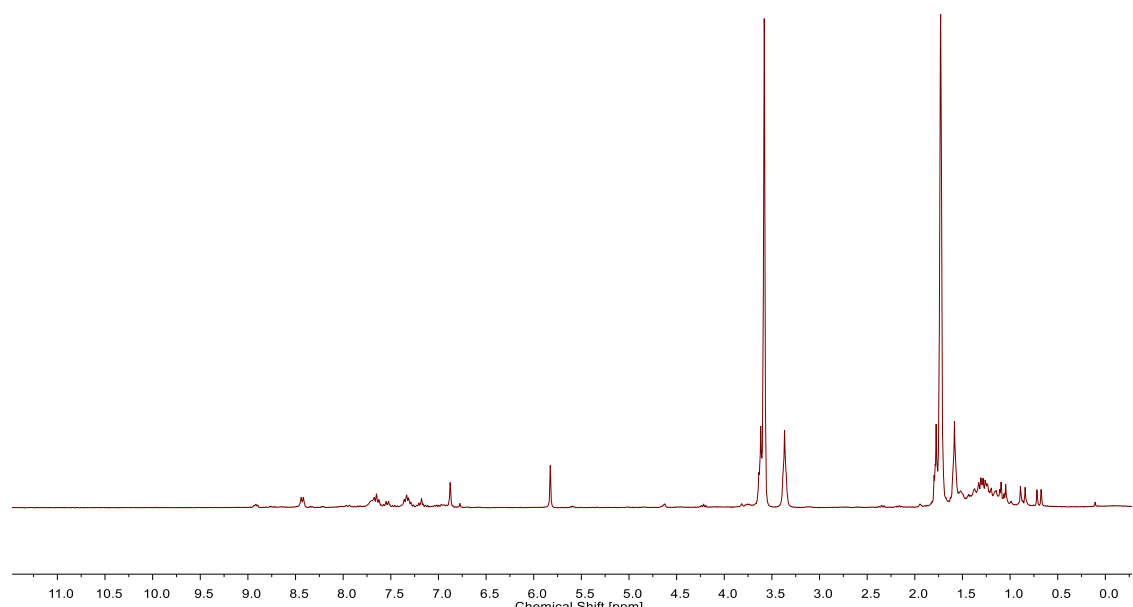


Figure S23. ¹H NMR spectrum of the reaction of **9** with **7**. The spectrum was recorded at r.t. using THF-d₈ as a solvent.

References

1. J. Abbenseth, M. Diefenbach, S. C. Bete, C. Würtele, C. Volkmann, S. Demeshko, M. C. Holthausen and S. Schneider, *Chem. Commun.*, 2017, **53**, 5511.
2. Gaussian 16, Revision B.01, M. J. Frisch, G. W. Trucks, H. B. Schlegel, G. E. Scuseria, M. A. Robb, J. R. Cheeseman, G. Scalmani, V. Barone, G. A. Petersson, H. Nakatsuji, X. Li, M. Caricato, A. V. Marenich, J. Bloino, B. G. Janesko, R. Gomperts, B. Mennucci, H. P. Hratchian, J. V. Ortiz, A. F. Izmaylov, J. L. Sonnenberg, D. Williams-Young, F. Ding, F. Lipparini, F. Egidi, J. Goings, B. Peng, A. Petrone, T. Henderson, D. Ranasinghe, V. G. Zakrzewski, J. Gao, N. Rega, G. Zheng, W. Liang, M. Hada, M. Ehara, K. Toyota, R. Fukuda, J. Hasegawa, M. Ishida, T. Nakajima, Y. Honda, O. Kitao, H. Nakai, T. Vreven, K. Throssell, J. A. Montgomery Jr., J. E. Peralta, F. Ogliaro, M. J. Bearpark, J. J. Heyd, E. N. Brothers, K. N. Kudin, V. N. Staroverov, T. A. Keith, R. Kobayashi, J. Normand, K. Raghavachari, A. P. Rendell, J. C. Burant, S. S. Iyengar, J. Tomasi, M. Cossi, J. M. Millam, M. Klene, C. Adamo, R. Cammi, J. W. Ochterski, R. L. Martin, K. Morokuma, O. Farkas, J. B. Foresman and D. J. Fox, Gaussian, Inc., Wallingford, CT, 2016.